Journal of Nuclear Materials 407 (2010) 178–188

Contents lists available at ScienceDirect

Journal of Nuclear Materials

journal homepage: www.elsevier.com/locate/jnucmat

Interface enabled defects reduction in helium ion irradiated Cu/V nanolayers

E.G. Fu [a,b], A. Misra [b], H. Wang [c], Lin Shao [d], X. Zhang [a,*]

[a] Department of Mechanical Engineering, Materials Science and Engineering Program, Texas A&M University, College Station, TX 77843-3123, United States
[b] Materials Physics and Applications Division, Los Alamos National Laboratory, Los Alamos, NM 87545, United States
[c] Department of Electrical and Computer Engineering, Texas A&M University, College Station, TX 77843-3128, United States
[d] Department of Nuclear Engineering, Texas A&M University, College Station, TX 77843-3133, United States

ARTICLE INFO

Article history:
Received 21 June 2010
Accepted 8 October 2010

ABSTRACT

Sputter-deposited Cu/V nanolayer films with individual layer thickness, h, varying from 1 to 200 nm were subjected to helium (He) ion irradiation at room temperature. At a peak dose level of 6 displacements per atom (dpa), the average helium bubble density and lattice expansion decrease significantly with decreasing h. The magnitude of radiation hardening decreases with decreasing individual layer thickness, and becomes negligible when h is 2.5 nm or less. This study indicates that nearly immiscible Cu/V interfaces spaced a few nm apart can effectively reduce the concentration of radiation induced point defects. Consequently, Cu/V nanolayers possess enhanced radiation tolerance, i.e., reduction of swelling and suppression of radiation hardening, compared to monolithic Cu or V.

1. Introduction

Radiation induced defects and evolutions of mechanical properties in neutron and ion irradiated metallic materials have been extensively studied [1–7]. During radiation the interactions between the energetic projectile particles and the atoms of the irradiated materials lead to atomic displacement damages, such as vacancies, interstitials, and their agglomerations in the form of vacancy clusters, voids and dislocation loops [8–12]. Stacking fault tetrahedra (SFT) as a result of agglomeration of vacancies is frequently observed in numerous irradiated metals and alloys with faced-centered cubic (FCC) structure, such as Au, Cu, Ni, Pd and austenitic stainless steel [13–19]. A high concentration of vacancy clusters and SFTs is observed in FCC Cu, whereas interstitial loops seem to prevail in irradiated body-centered cubic (BCC) V [20]. In fusion reactors, besides the aforementioned displacement damages, a high concentration of He atoms created via (n, α) or other transmutation reactions typically leads to a large number of He bubbles in irradiated structural metals [21–23]. Radiation induced void swelling can cause significant dimensional instability and degrade the mechanical properties in the form of embrittlement. Significant void swelling has been observed in neutron radiated 316L stainless steels [4]. Radiation hardening has been extensively studied in irradiated FCC and BCC monolithic metals, such as Cu and V [24–33]. In general, radiation hardening is substantial when metals are irradiated at temperature below 0.3–0.4 T_m, where T_m is the melting temperature [32]. The yield strengths of neutron irradiated Cu and V both increase with the extent of damage, displacement-per-atom (dpa). The increase of yield strength is approximately 200–300 MPa in bulk coarse-grained Cu and V irradiated at a damage level of ~1 dpa [34].

Microstructural control has been shown to be effective in suppressing radiation damage. Significant reduction of void swelling has been recognized in a series of ferritic/martensitic (F/M) steels [35–39] with BCC or body-centered tetragonal (BCT) structures. Also, oxide-dispersion-strengthened (ODS) alloys, with nanoscale oxides uniformly distributed in F/M steels, have shown superior void swelling resistance and high temperature thermal stability [40]. A high density of dislocations in cold-worked 316L stainless steel can moderately alleviate void swelling at low temperatures [3]. The aforementioned studies have shown that grain or phase boundaries may act as sinks for radiation induced point defects and their clusters, where recombination of interstitial and vacancy could occur and such recovery process assists the interfaces in maintaining their ability to continuously absorb point defects [41–44]. Singh [45] has shown that in austenitic stainless steels with grain size of 0.5–50 μm, smaller grains can effectively reduce the concentration of voids and void swelling. Furthermore, Singh and Foreman [46] have shown that the supersaturation of vacancy within grains is lower when grain size is smaller since grain boundaries are effective sinks to reduce radiation induced point defect density. Analytical work also shows that the sink strength of grain boundaries increases with decreasing grain sizes [47]. Increasing the volume fraction of grain or phase boundaries thus appears beneficial to alleviating radiation induced damage. Metallic nanolayer films possess very large interfacial areas. Recent studies show that immiscible Cu/Nb nanolayers, particularly those with a layer thickness of a few nm, are extremely resistant against He ion irradiation induced intermixing [48]. He bubbles are barely

* Corresponding author. Tel.: +1 979 845 2143; fax: +1 979 845 3081.
E-mail address: zhangx@tamu.edu (X. Zhang).

0022-3115/$ - see front matter © 2010 Elsevier B.V. All rights reserved.
doi:10.1016/j.jnucmat.2010.10.011

detectable in irradiated Cu/Nb 2.5 nm nanolayers, suggesting the extraordinary capability of Cu/Nb interface in reducing point defect concentration compared to their bulk counterparts [49]. Atomistic simulations show that pairs of extended jogs formed by misfit dislocations along interfaces can effectively lower the point defect formation energy, and such interfaces become virtually inexhaustible sinks for point defects and catalysts for efficient Frenkel pair recombination [50]. Molecular dynamics simulations of 5 keV displacement cascades near cube-on-cube Cu/Ni interfaces show that the total number of defects (vacancies and interstitials) in coherent Cu/Ni is considerably less than those in the pure Cu and Ni [51].

Despite these studies, the effect of the volume fraction of interfaces on radiation induced evolutions of microstructure and mechanical properties has not been studied systematically. In a recent letter, we reported preliminary studies of the reduction of He bubble density and suppression of radiation hardening in He ion irradiated Cu/V nanolayers [52]. Cu and V are selected because they are nearly immiscible and hence Cu/V interface could possess chemical stability under radiation. In this article, we provide a complete analysis of radiation (at room temperature) induced defects, lattice distortion, swelling, and evolution of hardness, and explain the mechanisms that lead to enhanced radiation tolerance in nearly immiscible Cu/V nanolayers. Although void swelling in metals typically occurs during radiation at elevated temperatures, radiation experiments in this study were all performed at room temperature so that we can investigate the role of immiscible layer interface on defect migration and annihilations by isolating the influence of other parameters, such as radiation temperature.

2. Experimental

Cu/V nanolayer films with equal individual layer thickness ranging from 1 to 200 nm were synthesized on HF etched Si (1 0 0) substrates by using DC magnetron sputtering at room temperature. The deposition rate was approximately 1 nm/s. The total thicknesses of Cu/V nanolayers were kept at 1.5–2 μm. A base pressure of 6.6×10^{-6} Pa was reached prior to depositions and argon partial pressure during sputtering was ~0.5 Pa. Before helium (He) ion irradiation, the samples with 5 × 10 mm in dimension were partially masked to avoid ion irradiation in the masked regions. After irradiation experiments, the difference in the height (step height) between the irradiated and the unirradiated regions was measured by using a Dektak 3 Stylus profilometer with a Z height resolution of better than 1 nm. Swelling is estimated as the ratio of the step height divided by the ion range (~400 nm) in the current studies. The ion irradiations were performed at room temperature using 50 keV He ions. A total fluence of $6 \times 10^{20}/m^2$ was achieved in 4 h at a constant beam current of 2 μA. Base pressure in the ion implanter was less than 1×10^{-5} Pa. The temperature rise of specimens due to beam heating was measured to be less than 50 °C. The temperature increase, ΔT, also can be estimated by [53]:

$$\Delta T = \frac{2J}{k_T}\left(\frac{k_T t}{\rho C_T}\right)^{1/2} \quad (1)$$

where J is beam power density in the unit of W/cm^2, k_T is thermal conductance in the unit of W/cm K, t is time, ρ and C_T are density and specific heat (W s/g K), respectively. For simplicity, in this study we use the thermal properties of Cu for estimation, and ΔT is estimated to be ~17 K.

The microstructure of Cu/V nanolayer films was characterized by Bruker-AXS D8 advanced Bragg–Brentano X-ray powder diffractometer (XRD). The cross-section transmission electron microscopy (XTEM) samples of the Cu/V nanolayers, prepared by dimpling and low energy (3.5 keV) Ar ion milling with a 5° incidence angle, were examined by a 200 kV JEOL 2010 transmission electron microscope equipped with a Gatan SC1000 ORIUS CCD camera. During TEM sample preparation Ar ion milling can induce damage in the form of Ar bubbles and amorphization. These artifacts were typically observed in a narrow region, within 20 nm from the edge of TEM specimens (near the center of a hole in specimens). Proper handling of ion milling parameters during TEM sample preparation (by using low energy, low angle ion milling), can effectively reduce the ion milling induced damage and evidence is given in Fig. 2e later in the results section. The scanning transmission electron microscopy (STEM) and energy dispersive X-ray (EDX) analysis for identifying the elemental composition and the interface integrity of the specimens were performed by the FEI Tecnai G2 F20 with Fischione ultra-high resolution STEM HAADF detector (0.23 nm in the STEM image mode) and Oxford instruments EDX detector with a spatial resolution of ~1 nm. The hardness and the indentation modulus of the films were measured based on an average of 9–12 indents at different indentation depths at room temperature, by a Fischerscope HM2000XYp micro/nanoindenter using a Vickers indenter with the same loading rate. Loading rate in HM2000XYp micro/nanoindenter is defined by square root maximum load divided by the time to reach maximum load. The loading rate was kept at 10 mN/s for all measurements. Hardness and indentation modulus were measured as a function of indentation depth, up to a maximum depth of ~200 nm for all specimens.

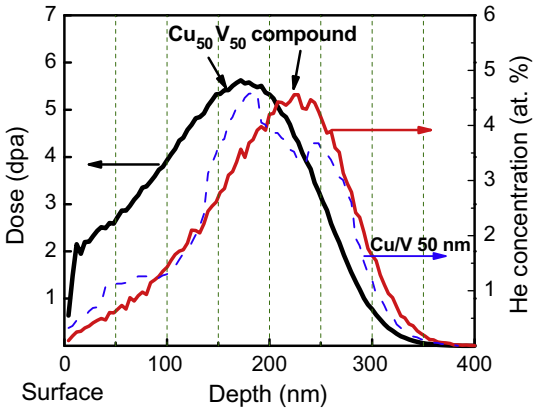

Fig. 1. The depth profile of radiation damage (in units of displacements per atom (dpa)) and helium concentration obtained from SRIM simulation of $Cu_{50}V_{50}$ compound subjected to He ion irradiation at 50 keV with a total fluence of 6×10^{20} ions/m^2. The depth profile of He concentration from SRIM simulation for Cu/V 50 nm multilayer is shown as well (dashed line). The simulated depth dependent He concentration profiles in Cu–V compound and Cu/V 50 nm nanolayers are similar.

3. Results

3.1. SRIM simulation

The stopping and range of ions in matter (SRIM) computer program based on Monte Carlo method [54] was used to compute the depth profile of He concentration and radiation damage (displacements per atom) in $Cu_{50}V_{50}$ compound irradiated by He ions at an energy of 50 keV and a total fluence of 6×10^{20} ions/m^2. The SRIM was also applied to Cu 50 nm/V 50 nm (referred to as Cu/V 50 nm thereafter) nanolayers as shown in Fig. 1, and Cu/V 5 nm nanolayers. The depth dependent He concentration profile is similar in both cases. The threshold displacement energy for Cu and V is 29 and 39 eV, respectively [55]. One major drawback of using layered morphology is that the simulation of Cu/V 5 nm nanolayer does not provide a complete depth dependent spectrum of He concentration

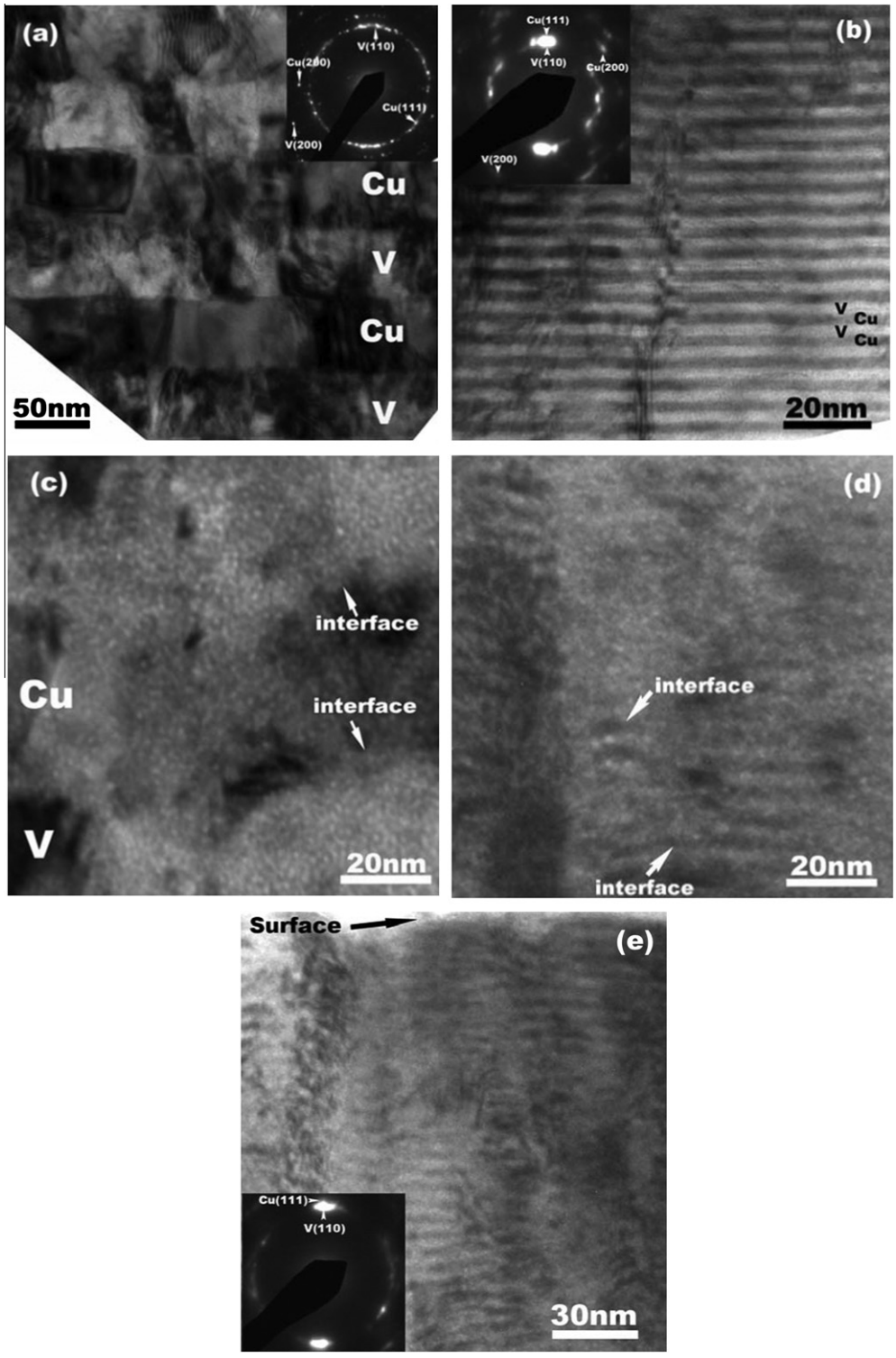

Fig. 2. Cross section TEM (XTEM) images of as-deposited (a) Cu/V 50 nm, and (b) Cu/V 2.5 nm nanolayers. Films with smaller individual layer thickness (h) have a stronger Cu {1 1 1} and V {1 1 0} fiber texture. (c) and (d) Peak damage regions of irradiated Cu/V 50 nm and Cu/V 2.5 nm nanolayers, respectively. He bubbles are observed in both Cu and V. (e) XTEM of ion irradiated Cu/V 2.5 nm films taken at under-focus condition shows that He and/or Ar bubbles are not detectable in a region within 150 nm from surface.

(limited by the SRIM program). Hence we will use $Cu_{50}V_{50}$ compound for the purpose of SRIM simulation thereafter. The simulation, as shown in Fig. 1, predicts that, in $Cu_{50}V_{50}$ compound, He concentration initially increases with the increase of the penetration depth, reaches a peak value of ~4.6 at.% at a depth of ~230 nm, and decays thereafter. The peak damage induced by He collisions in the compound is approximately 5.6 dpa at a depth of ~170 nm, and the radiation damage extends to a maximum depth of ~380 nm underneath the film surface upon 50 keV He ion irradiation.

3.2. Evolutions of microstructures examined by TEM

Bright field XTEM micrographs of the as-deposited and ion irradiated and Cu/V 50 nm and Cu/V 2.5 nm nanolayers are compared in Fig. 2. For all layer thicknesses, the as-deposited Cu/V nanolayers

possess polycrystalline columnar grain structures with clearly defined layer interfaces and Kurdjumov–Sachs (K–S) orientation relationship: Cu {1 1 1} // V {1 1 0} // interface, and Cu ⟨1 1 0⟩ // V ⟨1 1 1⟩. The columnar grain size, defined as the in-plane grain size of Cu and V in each layer, in as-deposited Cu/V 50 nm is on the order of the individual layer thickness, h, whereas the columnar grain size is much greater than h in the as-deposited Cu/V 2.5 nm specimen. Cu/V 2.5 nm nanolayers have stronger fiber texture of Cu {1 1 1} and V {1 1 0} than that of Cu/V 50 nm nanolayers. Sputter-deposited films have very good uniformity in terms of layer thickness. This is clearly seen in TEM micrographs. With computer controlled deposition, the deposition rate and time for each layer is the same, thus there is no variation in layer thickness. After He ion irradiation, de-focused XTEM experiments were performed to reveal microstructure evolution induced by He ion irradiation across the entire thickness of the Cu/V 50 nm and Cu/V 2.5 nm specimens. Lower-magnification de-focused bright field XTEM images across the entire radiation region [52] indicate that the number of He bubbles follows the concentration profile shown in Fig. 1 reaching a maximum at a depth of ~200 nm underneath the film surface. Selected area diffraction (SAD) patterns in irradiated Cu/V nanolayer indicate insignificant change of fiber textures. The microstructures of the Cu/V 50 nm and the Cu/V 2.5 nm specimens at the peak damage regions are shown in Fig. 2c and 2d. Comparisons of the two micrographs show similar size of He bubbles, ~1 nm in diameter, and the density of He bubbles in the irradiated Cu/V 50 nm specimen is much greater than that in the irradiated Cu/V 2.5 nm specimens. The He bubbles had a fairly uniform diameter (~1 nm) with narrow size distribution as shown by our extensive TEM studies. We did not detect any significant variation in bubble size as a function of distance from the layer interface. It is likely that interface may have accumulated a high concentration of He. But accurate determination of He concentration with nm spatial precision is still a major challenge. Available ion beam techniques can only provide an average He concentration across ion implantation path. Analytical transmission electron microscopy technique cannot detect He well. Fig. 2e shows that no obvious He and/or Ar bubbles are detectable in a region within ~150 nm from the surface in irradiated Cu/V 2.5 nm films. But He bubbles appear in deeper regions shown in Fig. 2d. The micrograph confirms that Ar ion milling damage (in the form of Ar bubbles) has been effectively minimized during our TEM sample preparation.

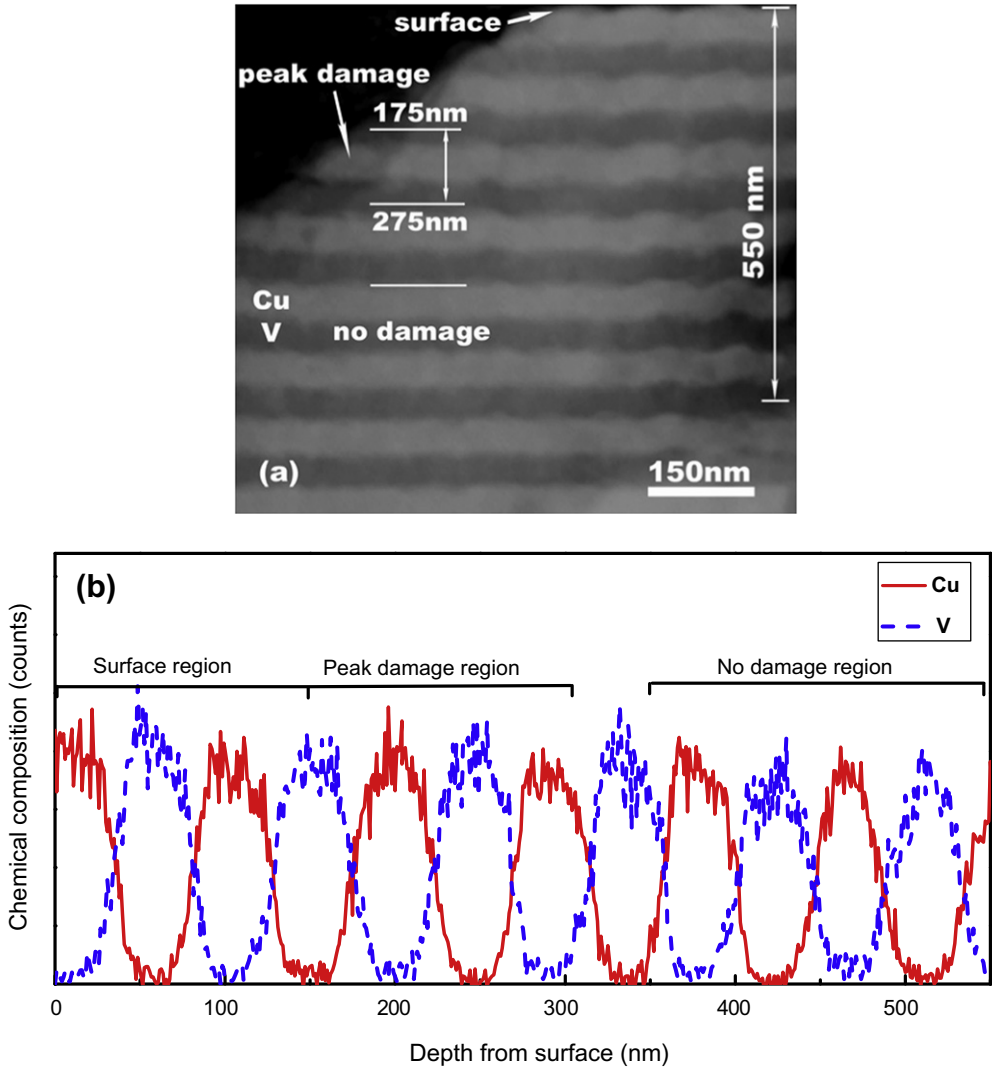

Fig. 3. (a) An STEM image of He ion irradiated Cu/V 50 nm nanolayers with a total fluence of 6×10^{20} ions/m^2. Abrupt interfaces are retained after radiations. (b) Semi-quantitative EDX chemical analysis along a 550 nm long line from the film surface as shown in 3(a), normal to the layer interface across all three regions: the surface, peak damage and no damage region. Radiation induces insignificant change in the modulated composition profiles.

3.3. Evolutions of microstructure examined by STEM technique and chemical analyses

STEM experiments were performed to examine the chemical integrity of layer interface after irradiation, since STEM is known to resolve different elements due to their difference in atomic numbers. A STEM micrograph of an ionirradiated Cu/V 50 nm specimen is shown in Fig. 3a. The brighter layers are Cu, sandwiched by the darker V layers. Three different regions predicted by SRIM simulation were examined: (i) a surface region with low-to-medium damage, (ii) a peak damage region at a depth of approximately 200 nm, and (iii) a no damage region that is deeper than the ion range. Chemically abrupt layer interfaces were observed in all three regions with the interfaces in the peak damage region being rougher than those in less irradiated or unirradiated regions. Furthermore, semi-quantitative chemical composition analysis via EDX was performed in the same specimen along a straight line, 550 nm in length as shown in Fig. 3a, normal to the layer interface across all three regions. The spot size of electron convergent beam is approximately 1 nm and the step size of the line scan is ~1 nm/step. As shown in Fig. 3b, the composition profiles for the three regions are essentially the same (no discernable sign of intermixing), indicating that radiation induced inter diffusion across layer interface, if any, is under the spatial resolution limit of such a technique. Similarly, the geometric and chemical integrity of the interfaces of the irradiated Cu/V 2.5 nm in the unirradiated and peak damage regions are compared in Fig. 4a and 4b. The comparison of STEM micrographs shows qualitatively that layer interfaces remain chemically modulated after He ion irradiation. In Fig. 4a the unirradiated region is close to the substrate surface and hence appears smoother, whereas the radiated region is close to the film surface and appears rougher due to island growth and the existence of residual stress. These phenomena are typically observed in many sputtered nanolayer films. Chemical analyses of the same specimen with an EDX spatial resolution of 1–2 nm are shown in Fig. 4c. Insignificant change in the peak-to-valley distances indicates that layer interfaces in the Cu/V 2.5 nm specimens were essentially unchanged after ion irradiation.

3.4. He bubbles and swelling measurements

XTEM was used to examine the influence of layer thickness on bubble density in ionirradiated Cu/V nanolayers. Several regions (typically 5) at the same depth were measured to examine the bubble density (from bright field images), and the results are then used to obtain average values and deviations. Fig. 5a shows He bubble density as a function of depth from the film surface in irradiated Cu/V 50 nm and Cu/V 2.5 nm nanolayers. He bubble density (number per unit volume) was calculated from TEM micrographs taken at an under-focus condition (−400 nm) where similar bubble sizes (~1 nm) are observed in all irradiated specimens. The thickness of electron beam transparent TEM thin metal foils is typically in the

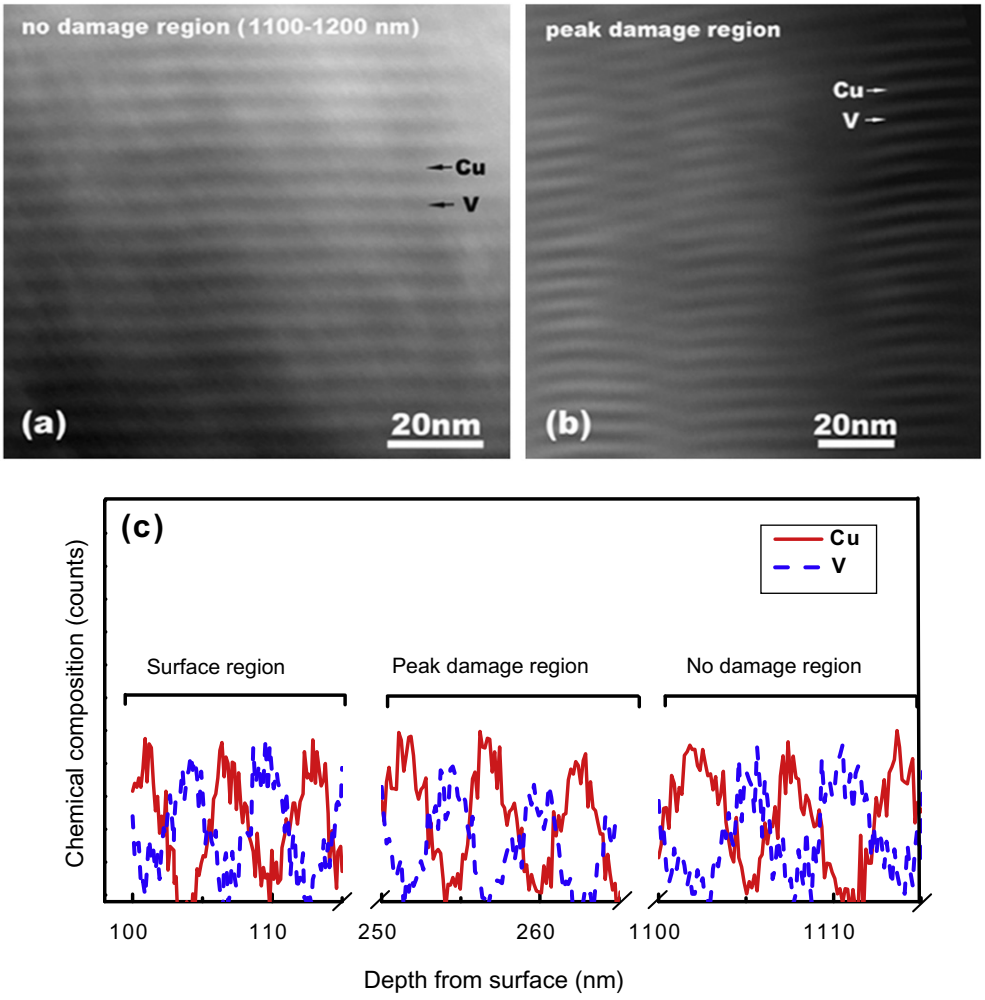

Fig. 4. STEM images of ion irradiated Cu/V 2.5 nm nanolayers in (a) a no damage region (~1100–1200 nm from surface), (b) a peak damage region (200–325 nm), and (c) EDX chemical analysis of the same specimen along the interface normal direction across three regions: the close-to-surface, peak damage and no damage region.

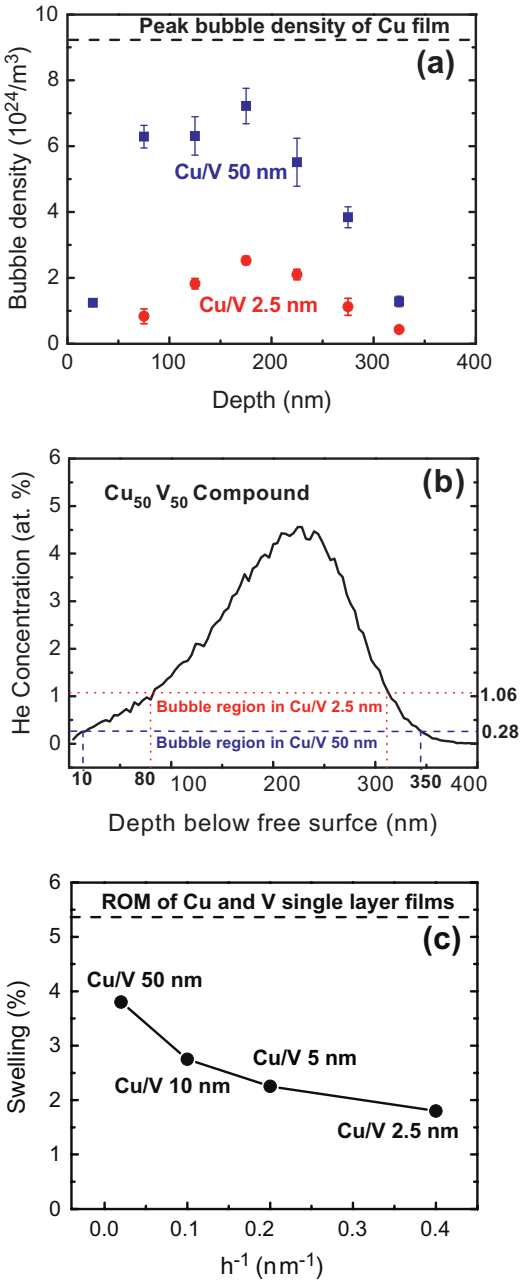

Fig. 5. (a) Comparison of He bubble density distributions along film normal direction underneath the surface in ion irradiated Cu/V 2.5 nm and Cu/V 50 nm nanolayers. Peak He bubble density is reduced by a factor of ~3 in Cu/V 2.5 nm, compared to that in Cu/V 50 nm specimens. (b) The minimum He concentration at which He bubbles are detectable in Cu/V 2.5 nm is ~4 times greater than that in Cu/V 50 nm nanolayer. Also shown is SRIM simulation of depth profile of He concentration for $Cu_{50}V_{50}$ compound subjected to He ion irradiation at 50 keV with a total fluence of 6×10^{20} ions/m^2. (c) Swelling vs. $1/h$ in ion irradiated Cu/V nanolayers, where h is individual layer thickness, shows a continuous swelling reduction with decreasing layer thickness. The rule-of-mixture (ROM) swelling in irradiated Cu and V single layer films is also shown by the horizontal dash line.

range of 10–50 nm, and hence the average TEM specimen thickness is estimated to be ~25 nm. In both cases, the He bubble density increases rapidly to a maximum at a depth of ~200 nm, where the helium concentration reaches a peak as shown in Fig. 1. One major difference in the two cases is that the peak He bubble density in the Cu/V 50 nm nanolayer is ~ three times greater than that of Cu/V 2.5 nm specimen. On the other hand, the peak bubble density of irradiated Cu/V 50 nm nanolayer specimens is still lower than that of single layer polycrystalline Cu films, as shown by the horizontal dashed line in Fig. 5a, irradiated at the same condition. From the XTEM studies, we also attempted to estimate the threshold concentration of He that leads to the formation of visible He bubbles. Fig. 5b shows the SRIM simulation of depth dependent He concentration profiles of $Cu_{50}V_{50}$ compound. The vertical dotted and the dashed lines, obtained from the TEM images, indicate the depth range over which bubbles are obviously observed in TEM images of irradiated Cu/V 2.5 nm and 50 nm nanolayers. The intersections of the vertical lines with the SRIM simulation show that a minimum He concentration to form detectable bubbles is approximately 1 at.% in Cu/V 2.5 nm at ~80 nm underneath the surface, and ~0.28 at.% in Cu/V 50 nm nanolayer at 10 nm from surface, with the surface layer being Cu. We observed similar values (~10 nm) in both single layer Cu and V irradiated at the same condition.

To provide a rough estimation of radiation induced swelling, the step height across the irradiated and unirradiated (no radiation) region was measured by a profilometer and the results are shown in Fig. 5c. The magnitude of swelling in nanolayers clearly decreases with decreasing h. The swelling in irradiated Cu/V 2.5 nm nanolayer is approximately two times lower than that in Cu/V 50 nm nanolayers. Furthermore, swelling in all irradiated Cu/V nanolayers is less than rule-of-mixture (ROM) swelling in irradiated single layer Cu and V films, shown as the horizontal dash line in Fig. 5c. For single layer Cu and V films subjected to identical irradiations an average of the measured swelling, referred to as ROM swelling, was used as a reference.

3.5. Lattice distortions examined by X-ray and electron diffraction

All the as-deposited and irradiated samples were characterized by XRD, and V (1 1 0), Cu (1 1 1) and Si (4 0 0) (as a reference peak) diffraction peaks are present in all diffraction patterns. XRD patterns of as-deposited and irradiated Cu/V nanolayers with h of 50 and 2.5 nm are shown in Fig. 6. V (1 1 0) and Cu (1 1 1) peaks are well separated in Cu/V 50 nm specimen, but they overlap in Cu/V 2.5 nm nanolayer. The V (1 1 0) and the Cu (1 1 1) peaks in the irradiated Cu/V 50 nm nanolayers are shifted to lower angles by 0.45° and 0.06°, corresponding to ~1.1% and 0.13% of lattice expansion, respectively. The overlapped peaks in Cu/V 2.5 nm nanolayers show peak shift with the same trend (i.e. lattice expansion), but at a smaller magnitude (0.11% of lattice expansion) than those observed in the irradiated Cu/V 50 nm specimen.

Systematic SAD experiments were performed, with an aperture size of 100 nm in diameter, to examine the localized variation of lattice distortions along the irradiation path. Depth dependent lattice expansions, calculated from the average over 100 nm regions, are

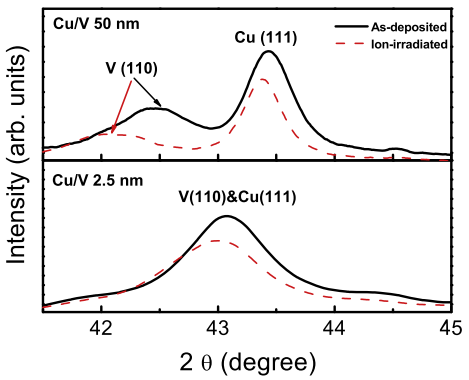

Fig. 6. XRD patterns of as-deposited and ion-irradiated Cu/V 50 nm and Cu/V 2.5 nm nanolayers. After radiation the peak intensity decreases and peak positions shift to lower angles.

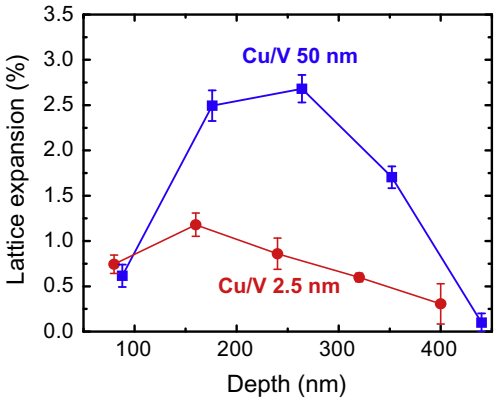

Fig. 7. The depth dependent evolution of lattice expansion of Cu/V 50 nm and 2.5 nm nanolayer films calculated from a series of SAD studies starting from the film surface. Diffraction was taken as an average of regions of ~100 nm in diameter, the smallest diameter of SAD aperture in the microscope.

shown in Fig. 7 for Cu/V 2.5 nm and Cu/V 50 nm nanolayers. The dependence of lattice expansions on implantation depth is similar to the variation of He bubble density vs. depth, as shown in Fig. 5a. The peak lattice expansion in Cu/V 2.5 nm specimens is ~1.2%, ~2–3 times lower than that in Cu/V 50 nm nanolayers, ~2.5%. The average lattice expansion is ~0.51% and 1.30% in Cu/V 2.5 nm and Cu/V 50 nm nanolayers, respectively. Both values are larger than those obtained by XRD studies, which yield the average lattice parameters of the whole specimen. Given the difficulty of distinguishing Cu (1 1 1) from V (1 1 0) in SADs, the average values of the two are used in the calculations. Overall, the XRD measurements are more precise in estimating the lattice strain, if specimens are uniformly strained through the thickness. The strains measured from SAD patterns, however, indicate the variation in strain with radiation depth, and show the correlation between the depth dependence of helium bubble density (Fig. 5a) and strain (Fig. 7).

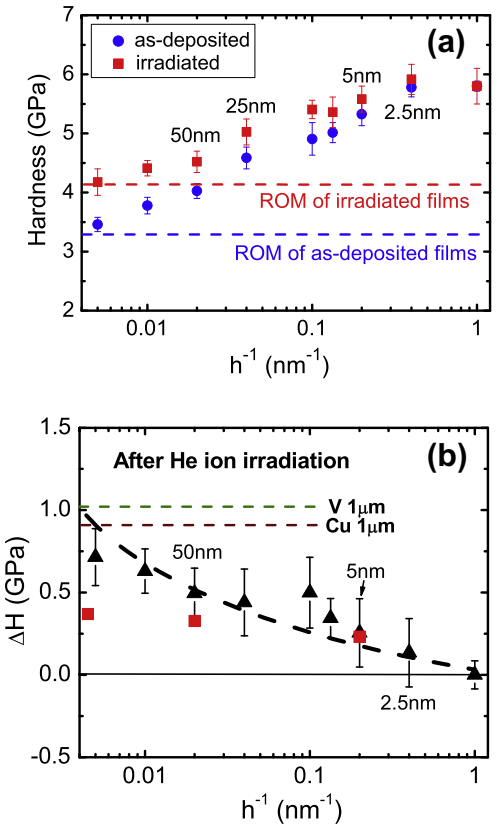

Fig. 8. (a) Comparison of hardnesses of as-deposited and ionirradiated Cu/V nanolayers as a function of h^{-1}. ROM hardness values of as-deposited and ion-irradiated films are also shown by horizontal dashed line, respectively. Hardnesses increase with decreasing h in both cases and approach peak values at h of 1–2.5 nm and (b) hardness variation ($\Delta H = H_{ion\text{-}irradiated} - H_{as\text{-}deposited}$) of Cu/V nanolayer after He ion irradiation as a function of h^{-1}. Radiation hardening in Cu and V single layer films is indicated by two horizontal dash lines. Radiation hardening of nanolayers (indicated by black triangle) increases with increasing h and approaches that of single layer Cu and V, and is negligible at h of 2.5 nm or less. Radiation hardening, estimated as three times calculated $\Delta\sigma$ indicated by squares, is shown in the figure to compare with experimental values.

3.6. Irradiation hardening

Hardnesses of as-deposited (shown by spheres) and ion-irradiated (shown by squares) Cu/V nanolayers vs. h^{-1} are plotted in Fig. 8a, where h is the individual layer thickness. The hardness of as-deposited Cu/V increases monotonically with decreasing h, and approach peak values at h of 2.5 nm or less. He ion irradiation in general leads to the increase of film hardness (radiation hardening). But the magnitude of radiation hardening diminishes continuously with decreasing h, and became negligible when $h \leqslant 2.5$ nm. To test the reproducibility of radiation hardening effect, two more sets of deposition, irradiation and hardness measurements were performed and results (not shown here) are reproducible. ROM hardness values of as-deposited and ion-irradiated films are also shown by horizontal dashed lines in the same plot, respectively, with an ROM hardness increase of ~1 GPa after irradiation. In order to examine hardness variation in more detail, the change of hardness between the as-deposited and ion irradiated Cu/V specimens, ΔH, as a function of h^{-1}, was plotted in Fig. 8b. The magnitude of ΔH (black triangle) increases with increasing h and approaches the values of radiation hardening in single layer Cu and V films (indicated by two horizontal dash lines, respectively).

4. Discussion

We will first examine the microstructure evolution, including the retention of layered morphology, generation of He bubbles and lattice distortions, and then the implication of these microstructural changes on irradiation hardening.

4.1. He solubility in nanolayers and morphological stability of Cu/V layer interfaces

In conventional bulk metallic materials, the solid solubility of He is extremely low [56]. In Cu/V nanolayers, He could be stored in crystal lattices, He bubbles and at layer interfaces or grain boundaries. Based on the observation of 1% He below which obvious He bubbles are not detectable (Fig. 5b), and the average columnar grain sizes are typically greater than individual layer thickness, we infer that interface plays a major role in significantly enhancing the solubility of He in metals.

An energetic ion beam can induce ion mixing at interfaces between dissimilar materials. Such energetic ion induced ballistic mixing can effectively induce the formation of new phases or even destroy layer interfaces in the miscible systems, such as Cu/Au [57], Hf/Ti [58], Fe/W [59] and Al/Nb [60]. Ion beam mixing has been studied in the past [53,61]. The cascade mixing can be described by an effective diffusivity D for a collision-cascade-induced random walk process with a diffusion equation expressed as [53]:

$$Dt = 0.067 \frac{F_D \langle r^2 \rangle}{N E_d} \varphi \qquad (2)$$

where t is effective diffusion time, F_D is nuclear stopping power, $\langle r^2 \rangle$ is the mean squared range of the displaced atoms in the target, φ is

ion dose, E_d is displacement energy, and N is atomic density. A reasonable value of 1 nm can be chosen to describe $\langle r^2 \rangle$ as discussed in Ref. [61]. This value is a good approximation since at very low energy, the mean travel distance of recoiled target atoms should be equal to mean lattice spacing which is about 1 nm. In the present study the peak damage is 5.6 dpa, the F_D for Cu at the peak damage position is ~57 eV/nm, and thus a rough estimation yields $Dt = 1\ \text{nm}^2$. This analysis predicts that, in Cu/V 2.5 nm nanolayers, significant ballistic intermixing should occur and may completely destruct the layer interface. In contrast the chemical stability of interface in irradiated nanolayers (as revealed by series of STEM studies) indicates that there is a strong demixing tendency at Cu/V layer interfaces. Cu/V system has a positive heat of mixing, ~5 kJ/mol [62], hence a chemically driven demixing process may have occurred simultaneously during irradiation (collision cascades). Similar phenomena have been observed in several other immiscible systems, such as Cu/W [57], Cu/Nb [48] and Hf/Ni [58]. The mutual solid solubility between Cu and V is very limited, approximately 2 at.% Cu in V matrix at 800 °C [63]. Intermixing at the level of a few at.% is below the detection limit of the STEM technique used in this study, The curvature of interfaces as shown in Fig. 4 is typically observed in TEM analyses of columnar grains [64], and is a consequence of the island growth mechanism of sputtered films.

4.2. Radiation induced He bubbles and lattice distortion

We now attempt to analyze radiation induced defect concentration and corresponding lattice distortion in nanolayers. The primary radiation damage event in crystalline metals is the displacement of one or more atoms, and consequently vacancies and self-interstitials are created and foreign elements are introduced in crystal lattices [65]. In bulk FCC metal with low-to-medium stacking fault energy (SFE), such as Cu ($\gamma_{SF} = 39\ \text{mJ/m}^2$) [19], approximately 90% of neutron radiation induced defects are stacking fault tetrahedra (SFT) at a density of $2\text{–}6 \times 10^{23}/\text{m}^3$ at a damage level of 0.01–0.9 dpa [20]. In BCC bulk V irradiated at 65–100 °C, radiation induced defects are mostly dominated by interstitial loops, 2 nm in diameter, at a density level of $1\text{–}2 \times 10^{23}/\text{m}^3$ [20,66]. Helium will rapidly combine with vacancies and vacancy clusters to form bubbles.

He bubbles have been observed in most irradiated Cu/V nanolayers. In most irradiated Cu/V nanolayers, He bubbles have an average diameter of ~1 nm, with very narrow and uniform distributions. Our analysis also indicates that the average bubble size depends very little on h of the nanolayers. The reduction of He bubble density in Cu/V 2.5 nm specimen by a factor of approximately 3–4 compared to that in irradiated Cu/V 50 nm and Cu films indicates that vacancy concentration must have been dramatically reduced.

It is generally accepted that radiation induced defects tend to migrate to the interfacial regions, such as grain boundaries and interfaces [45,46,67]. These interfacial regions are expected to act as effective sinks for radiation induced defects. The interfacial area density (number of interface per unit length along the direction normal to the layer interfaces) in Cu/V 2.5 nm nanolayers is 20 times higher than that in Cu/V 50 nm nanolayers. It is likely that defect migration along interface is facilitated, an event that leads to enhanced annihilation of opposite type defects. Recent MD simulation studies of Cu/Nb nanolayer films showed the formation energies of vacancies are significantly lower at Cu/Nb interfaces than those in the perfect crystals of the neighboring elements [68]. A lower defect formation energy at interface indicates that the equilibrium concentration of vacancies, Cv_o, can be higher at interface. And consequently interface can absorb much higher concentration of vacancies than in bulk before they reach supersaturation (which leads to the formation of He bubbles). No higher density of bubbles was observed at the interfaces. Additionally there are two other factors that make interface effective sinks for point defects. Pairs of extended jogs are formed by misfit dislocations along interfaces, and consequently such interfaces become virtually inexhaustible sinks for point defects and catalysts for efficient Frenkel pair recombination [50]. Thus vacancies and interstitials that migrate to the layer interface are effectively trapped and undergo accelerated recombination due to the enhanced diffusivity and effective size of interfacial point defects [68]. It is likely that when h in the nanolayer is reduced to a few nm length scale, the value of equilibrium vacancy concentration is slightly increased due to the interface effect. As a result the capacity of defect storage in nanolayer is enhanced and reduces the supersaturation of vacancies. A lower supersaturation of vacancies will delay or reduce the clustering of vacancies to form He bubbles. The reduction of He bubble density in nanolayers is thus suggested to be a combined effect of enhanced defect storage capacity (increasing equilibrium vacancy concentration) and increased probability of defect annihilation at interfaces (decreasing the overall concentration of vacancies).

Lattice expansion is observed in XRD and TEM–SAD analyses as shown in Figs. 6 and 7. There are several factors that may contribute to lattice distortions, including dissolution of solute atoms, vacancies, He bubbles, isolated interstitials, and interstitial loops. Isolated interstitials are mobile in FCC Cu at room temperature [69], and may migrate to interfaces or form loops, and hence significantly reduce the overall concentration of interstitials in nanolayers. Given their low concentration, the contribution of isolated interstitials to lattice expansion may be insignificant in nanolayers. Our HRTEM analyses (not shown here) have revealed certain interstitial loops, but an accurate determination of loop density in nanolayers is very challenging and not yet available. We have attempted to estimate interstitial loop density, in a later section, from radiation hardening studies, and the analysis shows that the contribution of dislocation loops to lattice expansion is negligible. From the Cu–V phase diagram [63], it is evident that up to 2.0 at.% of Cu can be dissolved in V. Assuming that ion irradiation induces slight intermixing by incorporating a maximum of 2 at.% Cu into V, and by using the lattice parameters of Cu and V ($a_{Cu} = 3.615$ Å $a_V = 3.027$ Å), one can estimate a lattice expansion of ~0.46% in V. However the peak lattice expansion is ~2.50% in Cu/V 50 nm nanolayers as revealed by SAD studies in Fig. 7. Also, the intermixing zone is unlikely to extend over several tens of nanometers given that the microscopy characterization (Figs. 3 and 4) revealed the preservation of discrete, compositionally modulated layered structure. In the ion irradiated Cu/V 50 nm specimen, the variations of He bubble density and lattice expansion with implantation depth follow a similar trend (i.e. a maximum at approximately 200 nm below the surface). This observation implies that pressurized He bubbles may account for much of the observed lattice expansion.

Pressurized He bubbles could lead to lattice expansion based on the point source dilatation mechanism [70]. The pressure due to point source (He bubbles in this case) dilatation can be expressed as:

$$P = \frac{\mu \delta v}{\pi r_0^3} \tag{3}$$

where μ is the shear modulus of the metal matrix, and δv is the volume expansion induced by internal pressure, and r_0 is the radius of bubbles. The peak lattice expansion is ~2.50% in Cu/V 50 nm nanolayers as revealed by SAD studies. A lattice expansion from solid solution is ~0.46% in V. If we assume that the lattice expansion due to He bubble is approximately 2% in V, which is the result of lat-

tice expansion measured from experiments subtracted by solid solution induced expansion (= 2.50−0.46%), given μ = 46 GPa for V and a bubble radius of 0.5 nm, the pressure is estimated to be ~3.8 GPa. By using the EOS of He [71,72], the molar volume of He is estimated to be 6.29 cm^3/mol, or approximately 1.3 He atoms per vacancy in V. A similar result, 1.1 He atoms per vacancy in Cu is obtained. This compares well with literature values (1.4 He/vacancy in He bubbles of 4 GPa pressure in V, and 1.0 He/vacancy in He bubbles of 2.8 GPa pressure in Cu [73]). In general vacancy clusters will induce negligible or slightly negative volume change. However, when vacancy clusters are filled with high density He to form over pressurized He bubbles, as is the case in this study; they will create lattice expansions, based on point source dilatation analysis. He bubble induced lattice expansions have been observed in numerous other systems, where the magnitude of lattice expansion is proportional to the He concentration [74,75]. The mechanism of tensile stress induced lattice expansion in regions between pressurized He bubbles has been established mathematically by Wolfer [75]. Given the estimated He molar volume, ~6.29 cm^3/mol, in Cu/V 50 nm nanolayer and use Cu as matrix, we derive that ~0.5 at.% of He is stored in these He bubbles. The peak He concentration estimated by SRIM simulation is ~4.6 at.% (Fig. 5b), hence a large number of He atom should reside at the interface as well as inside the matrix. Many small cavities in the form of He-vacancy clusters should exist below the resolution limit of the TEM technique, i.e. their diameter is less than 0.5 nm. These small He-vacancy clusters may also contribute to the lattice expansion observed experimentally, and consequently the aforementioned estimation of He pressure could be an upper bound value.

4.3. Mechanical integrity and hardening mechanisms

In conventional metals, radiation hardening is due to the interaction of dislocations with two types of radiation induced defects: strong obstacles such as interstitials, interstitial loops, SFT and precipitates, and relatively weak obstacles such as He bubbles [76]. In the MD simulation of irradiated Fe [65], it was shown that dislocation loops and small voids are stronger obstacles. He bubbles with 1–2 He/vacancy are weaker obstacles. However, the same simulation study also shows the barrier strength of He bubbles increases with increasing He/vacancy ratio (greater than 2). The interaction of glide dislocations with Cu/V interfaces is not expected to change significantly given the retention of chemically abrupt interfaces after radiation. The previous review article regarding obstacle-controlled strengthening showed that the dispersed barrier model [65,77] can explain strong obstacles induced hardening well. Whereas Friedel–Kroupa–Hirsch (FKH) model was developed to explain weak obstacles induced hardening [78,79]. The contribution of He bubbles to radiation hardening is negligible at low He concentration and becomes significant only above a critical He concentration around 1 at.% [80–82]. The SRIM simulation results predict that the average He concentration is greater than 1 at.% in Cu/V 5 nm and Cu/V 50 nm nanolayers. When the bubble size is very small, He bubble is treated as a weak obstacle. The FKH model is applied to estimate the He bubbles induced enhancement of yield strength, $\Delta\sigma$, by [65]:

$$\Delta\sigma = \frac{1}{8} M\mu b d N^{2/3} \tag{4}$$

where M is the Taylor factor. μ is the shear modulus with the value of 46 GPa for both Cu and V. b stands for the Burgers vector of the primary glide dislocations. For FCC polycrystals, the Taylor factor, M, averaged for different crystal orientations by Taylor, is 3.06 [83–84]. For BCC crystals, the Taylor factor on $\{1\,1\,0\}/\langle 1\,1\,1\rangle$ slip system is 3.067. In the current studies, there are BCC {1 1 0} texture in V films. And as pointed out by Kocks [85,86], for all physics situations of approximate pencil glide, where the {1 1 0} plane may be somewhat preferred, the average Taylor factor, is 2.9 ± 5%. Hence for simplicity, M was taken as 3 in Cu/V nanolayers with fcc/bcc interface. The magnitude of the Burgers vector in FCC Cu is $a_{Cu}/\sqrt{2} = 0.3615/\sqrt{2} = 0.25562$ nm, and it is $a_V\sqrt{3}/2 = 0.3027 \times \sqrt{3}/2 = 0.26218$ nm in BCC V. The diameter of He bubbles (d), ~1 nm, and their average number density (N) across the radiation damage region are obtained from TEM measurements. Radiation hardening, estimated as three times that of the calculated $\Delta\sigma$ [87] indicated by red square, is compared with experimental values (indicated by black triangles) in Fig. 8b for $h \geqslant 5$ nm. It should be noted that when h, is 2.5 nm or less, the strength of nanolayers before radiation typically reaches a maximum value and is independent of layer thickness. This is because that the strength at h of 1–2 nm is determined by interface cutting stress in the absence of dislocation pileups as shown in Cu/Nb nanolayers with immiscible fcc/bcc interface [88]. The addition of point defects and their clusters is relatively weaker barrier to dislocations compared to that the resistance of interface. Hence radiation induced defects at low density is less likely to enhance the resistance to the transmission of dislocations across interface. However if the density of these point defects is sufficiently high, their contribution to radiation hardening may still need to be considered in fine nanolayers. In spite of a good comparison with experimental results at h = 5 nm, He bubble induced hardening alone, in general, clearly underestimates the experimental values for single layer Cu and V film, and nanolayers with greater h (h = 50 nm for instance). Other factors, such as He-vacancy clusters (less than 0.5 nm) and interstitial loops may also contribute to hardening. But since He-vacancy clusters are likely to be much weaker barriers than He bubbles, their contribution to hardening will not be considered further in this study.

We noticed that, in spite of a rather high He bubble density, the average distance between He bubbles (λ, estimated as $1/\sqrt{Nd}$[8]) is ~25 nm, a length scale where Orowan type of dislocation bowing between bubbles is a reasonable mechanism. Depending on the difference between inter bubble separation (λ) and h, radiation hardening in nanolayers could be categorized into three regimes. (i) For $h \ll \lambda$, at a few nm length scale, the yield strength of the nanolayers is expected to be controlled by the smaller length scale, h, with minimal contribution from He bubbles. (ii) When h is comparable to λ, radiation hardening from bubbles will become more evident. (iii) Finally when h is much greater than λ, on the order of hundreds of nm, the magnitude of radiation hardening approaches that of single layer films, and significant hardening by irradiation induced defects is expected. In addition to He bubbles, other defects, such as interstitial loops will also become important. At small h, interstitials are expected to migrate to interface sinks and hence, loops may not form within layers, or the loop density is too low to induce any significant hardening.

Interstitial loops are typically treated as strong barriers to the glide of the dislocations. A dispersed barrier model is developed to estimate strengthening due to interstitial loops. The variation (increase) in yield strength, $\Delta\sigma$, after radiation, is expressed by:

$$\Delta\sigma = M\alpha'\mu b\sqrt{Nd} \tag{5}$$

where M, μ, b, N and d carry the same physical meanings as defined previously in Eq. (4), but this time the defect clusters are interstitial loops. α' is a parameter that depends on the average barrier strength of the radiation induced defect clusters. Recent studies estimate that α' is 0.26 for V, and 0.2 for Cu [20]. Although HRTEM studies (not shown here) have revealed the formation of interstitial loops in irradiated Cu/V nanolayers, a clean measurement of loop density in nanolayers has proven difficult. From radiation hardening studies, we can infer indirectly the density of dislocation loops. By subtracting the contribution of He bubble induced hardening from the

measured values, the average interstitial loop density with an assumption of size of 2 nm is estimated as $5 \times 10^{22}/m^3$ for Cu/V 50 nm nanolayer. This is an order of magnitude lower than the interstitial loop density of $6.7 \times 10^{23}/m^3$ and $2.3 \times 10^{23}/m^3$ in neutron-irradiated polycrystalline pure Cu and V metals subjected to a total dose of 0.92 and 0.69 dpa, respectively [20]. The size of dislocation loops is roughly estimated to be ~2 nm based on high resolution TEM studies of irradiated Cu/V nanolayers. This loop size is also consistent with that observed in Cu irritated by neutron at temperature of 60–100 °C [20]. The HRTEM micrograph was not shown because interstitial loops are observed only when the nanolayers are oriented perfectly in zone. So their density appears low. Quantitative comparison of loop density evolution before and after radiation in nanolayers with nanograins is still a challenge. Detailed characterization of dislocation loops in irradiated Cu/V nanolayers will be performed in future study.

The lattice expansion, $\Delta a/a$, where a is the lattice parameter, due to dislocation loops can be estimated by [89,90]:

$$\frac{\Delta a}{a} = \frac{1}{3}\frac{\Delta V}{V} = \frac{\pi b n_l d_l^2}{12} \quad (6)$$

where $\Delta V/V$ is the fraction of volume change induced by defects, and $\Delta V = \pi b n_l (d_l/2)^2$, b is the Burgers vector of dislocation loop, n_l and d_l represent loop density and diameter, respectively. Using the estimated loop density of $5 \times 10^{22}/m^3$, loop diameter of 2 nm, and $b = 0.26$ nm, the lattice expansion is estimated to be 1.4×10^{-5}, negligible comparing to the measured expansion (Fig. 7) of 0.5–2.5%. Although dislocation loop density is insufficient to induce obvious lattice expansion, they may contribute considerably to radiation hardening given that loops are stronger obstacles to dislocations than He bubbles.

4.4. The significance of Cu/V interface in enhancing radiation resistance in nanolayers

Our study clearly demonstrates that in the nearly immiscible Cu/V system, layer interfaces play significant roles in enhancing radiation resistance of the nanolayers, manifested as reduced He bubble density and less radiation hardening. Based on this study the fundamental mechanisms of interface-driven enhancement of radiation tolerance can be interpreted as follows.

(1) Interfaces (between Cu and V) act as sinks for defects (vacancies, interstitials and helium atoms). As discussed previously the defect formation energy is lower at interfaces than in crystal lattices [68], and consequently the supersaturation of vacancies is reduced, which in turn will reduce or delay the clustering of vacancies or the formation of He bubbles. Furthermore MD simulations of Cu/Nb interface show that misfit dislocations evolve into extended jog pairs and significantly increase the sink capacity of Cu/Nb interfaces [50]. Since the immiscible Cu/V has a similar interface (fcc/bcc type with K–S orientation relationship) comparing to immiscible Cu/Nb, we anticipate that the Cu/V interface will also have high sink capacity for point defects.

(2) Interfaces promote annihilation of unlike defects since these defects have high mobility and delocalized cores [50] at interfaces. Recent MD simulation studies [50,73] have shown that interfaces will athermally absorb and annihilate point defects within 2 ps after their generation up to a distance of approximately 1–2 nm from the interface. With an interface spacing of 2.5 nm in Cu/V 2.5 nm nanolayers, the distance between cascade events and interfaces is expected to be small enough to allow direct interaction without the need for diffusion. So the annihilation process in these very fine nanolayers should occur almost instantaneously with the collision cascades. Whereas in bulk lattices, the interface-defect interactions will depends on both the length and time scales.

(3) Interfaces enabled enhancement of He solubility in metals. Comparing to the extremely low solid solubility of He in bulk metals, the observation that He bubbles are not detectable in Cu/V 2.5 nm nanolayers when He concentration is below 1 at.% strongly suggests that interface play an important role in significantly enhancing the He solubility in metals. He shall be distributed both in matrix (combined with vacancies) and at interfaces. There is no solid evidence on preferential segregation of He to layer interfaces at the moment.

(4) Interfaces in Cu/V nanolayers can significantly reduce the densities of defect clusters such as interstitial loops, SFT, and more importantly He bubbles, and hence, dramatically alleviate swelling and suppress irradiation hardening. Furthermore the significance of interface is also manifested from a clear size (layer thickness) dependent reduction of swelling and irradiation hardening. When h is ~100 nm or greater, the radiation tolerance of nanolayer decays and approaches that of bulk materials. The influence of radiation temperature and dose rate on size dependent radiation damage in nanolayers will be important subjects for future studies.

5. Summary and conclusions

The evolutions of microstructure and mechanical properties of sputtered Cu/V nanolayers subjected to 50 keV He ion irradiation were investigated systematically. Irradiated nanolayer interfaces remain chemically abrupt even in the peak damage region upon a total dosage of ~6 dpa. Such immiscible layer interface acts as sinks for point defects, and can effectively reduce the overall concentration of He bubbles and swelling, the magnitude of which reduces at smaller individual layer thickness. These nanolayers also show clearly a monotonic suppression of radiation hardening at smaller layer thickness due to the effective attraction and facilitated annihilation of Frenkel pair defects. Nanolayers with immiscible layer interface hence may offer a promising approach in alleviating swelling and radiation hardening.

Acknowledgements

XZ acknowledges financial support by US Army Research Office – Materials Science Division, under Contract No. W911NF-09-1-0223. AM acknowledges support by the US DOE, Office of Science, Office of Basic Energy Sciences. The authors also acknowledge discussions with Drs. J.P. Hirth and R.G. Hoagland. Support by Center for Integrated Nanotechnologies (CINT) under user agreement at Los Alamos National Laboratory is also acknowledged. The authors thank Dr. J. Carter and Drs. J.G. Swadener and Y.Q. Wang for conducting the He ion irradiation experiments at Texas A&M University and Los Alamos National Laboratory for reproducibility studies. E.G. Fu acknowledges the support from Consortium for Nanomaterials for Aerospace Commerce and Technology (CONTACT) program from Texas and the Air Force. We also acknowledge the usage of microscopes at the Microscopy and Imaging Center at Texas A&M University, and Mr. K. Baldwin and O. Anderoglu for their assistance in sputter-deposition of nanolayers.

References

[1] P.J. Maziasz, J. Nucl. Mater. 205 (1993) 118.
[2] L.K. Mansur, W.A. Coghlan, J. Nucl. Mater. 119 (1) (1983) 1.

[3] R.L. Klueh, N. Hashimoto, M.A. Sokolov, P.J. Maziasz, K. Shiba, S. Jitsukawa, J. Nucl. Mater. 357 (1–3) (2006) 169.
[4] F.A. Garner, M.B. Toloczko, B.H. Sencer, J. Nucl. Mater. 276 (2000) 123.
[5] A. Iwase, S. Ishino, J. Nucl. Mater. 276 (1–3) (2000) 178.
[6] H. Trinkaus, B.N. Singh, J. Nucl. Mater. 323 (2–3) (2003) 229.
[7] S. Ishino, J. Nucl. Mater. 251 (11) (1997) 225.
[8] G. Was, Fundamentals of Radiation Materials Science, Springer, New York, 2007.
[9] H. Ullmaier, Nucl. Fusion 24 (8) (1984) 1039.
[10] S.J. Zinkle, B.N. Singh, J. Nucl. Mater. 199 (3) (1993) 173.
[11] W.J. Phythian, R.E. Stoller, A.J.E. Foreman, A.F. Calder, D.J. Bacon, J. Nucl. Mater. 223 (3) (1995) 245.
[12] M.L. Jenkins, M.A. Kirk, W.J. Phythian, J. Nucl. Mater. 205 (1993) 16.
[13] Y. Dai, M. Victoria, Acta Mater. 45 (8) (1997) 3495.
[14] Y. Matsukawa, Y.N. Osetsky, R.E. Stoller, S.J. Zinkle, Philos. Mag. 88 (4) (2008) 581.
[15] M.L. Jenkins, Philos. Mag. 29 (4) (1974) 813.
[16] S.J. Zinkle, L.L. Snead, J. Nucl. Mater. 225 (1995) 123.
[17] B.N. Singh, A. Horsewell, P. Toft, D.J. Edwards, J. Nucl. Mater. 224 (2) (1995) 131.
[18] Y. Shimomura, R. Nishiguchi, Radiat. Eff. Defects Solids 141 (1–4) (1997) 311.
[19] R. Schaublin, Z. Yao, N. Baluc, M. Victoria, Philos. Mag. 85 (4–7) (2005) 769.
[20] N. Hashimoto, T.S. Byun, K. Farrell, S.J. Zinkle, J. Nucl. Mater. 329 (2004) 947.
[21] F.A. Garner, B.M. Oliver, L.R. Greenwood, M.R. James, P.D. Ferguson, S.A. Maloy, W.F. Sommer, J. Nucl. Mater. 296 (2001) 66.
[22] B.M. Oliver, M.R. James, F.A. Garner, S.A. Maloy, J. Nucl. Mater. 307 (2002) 1471.
[23] I.I. Chernov, A.N. Kalashnikov, B.A. Kahn, S.Y. Binyukova, J. Nucl. Mater. 323 (2–3) (2003) 341.
[24] S.A. Fabritsiev, A.S. Pokrovsky, Fusion Eng. Des. 65 (4) (2003) 545.
[25] N. Hashimoto, T.S. Byun, K. Farrell, J. Nucl. Mater. 351 (1–3) (2006) 295.
[26] M. Victoria, N. Baluc, C. Bailat, Y. Dai, M.I. Luppo, R. Schaublin, B.N. Singh, J. Nucl. Mater. 276 (2000) 114.
[27] K. Shiraishi, K. Fukaya, Y. Katano, J. Nucl. Mater. 54 (2) (1974) 275.
[28] E.R. Bradley, R.H. Jones, J. Nucl. Mater. 103 (1–3) (1982) 901.
[29] D. Kaletta, W. Schneider, J. Nucl. Mater. 122 (1–3) (1984) 418.
[30] H. Matsu, K. Abe, S. Hirano, O. Yoshinari, M. Koiwa, J. Nucl. Mater. 133 (August) (1985) 615.
[31] H. Takahashi, S. Ohnuki, H. Kinoshita, R. Nagasaki, K. Abe, J. Nucl. Mater. 155 (1988) 982.
[32] B.N. Singh, D.J. Edwards, P. Toft, J. Nucl. Mater. 299 (2001) 205.
[33] S.J. Zinkle, M. Victoria, K. Abe, J. Nucl. Mater. 307 (2002) 31.
[34] T.S. Byun, K. Farrell, J. Nucl. Mater. 326 (2–3) (2004) 86.
[35] R.L. Klueh, D.S. Gelles, S. Jitsukawa, A. Kimura, G.R. Odette, B. van der Schaaf, M. Victoria, J. Nucl. Mater. 307 (2002) 455.
[36] T. Hasegawa, Y. Tomita, A. Kohyama, J. Nucl. Mater. 258 (1998) 1153.
[37] A. Hishinuma, A. Kohyama, R.L. Klueh, D.S. Gelles, W. Dietz, K. Ehrlich, J. Nucl. Mater. 258 (1998) 193.
[38] R.L. Klueh, K. Ehrlich, F. Abe, J. Nucl. Mater. 191 (1992) 116.
[39] K. Ehrlich, K. Anderko, J. Nucl. Mater. 171 (1) (1990) 139.
[40] G.R. Odette, M.J. Alinger, B.D. Wirth, Annu. Rev. Mater. Res. 38 (2008) 471.
[41] M. Rose, A.G. Balogh, H. Hahn, Defect formation in irradiated nanostructured materials, in: A.G. Balogh, G. Walter (Ed.) Materials Science Applications of Ion Beam Techniques, 1997, p. 213.
[42] M. Rose, A.G. Balogh, H. Hahn, Nucl. Instrum. Methods Phys. Res. Sect. B – Beam Interact. Materi. Atoms 127 (1997) 119.
[43] Y. Chimi, A. Iwase, N. Ishikawa, A. Kobiyama, T. Inami, S. Okuda, J. Nucl. Mater. 297 (3) (2001) 355.
[44] M.T. Robinson, J. Nucl. Mater. 216 (1994) 1.
[45] B.N. Singh, Philos. Mag. 29 (1974) 25.
[46] B.N. Singh, A.J.E. Foreman, Philos. Mag. 29 (1974) 847.
[47] R. Bullough, M.R. Hayns, M.H. Wood, J. Nucl. Mater. 90 (1980) 44.
[48] T. Hochbauer, A. Misra, K. Hattar, R.G. Hoagland, J. Appl. Phys. 98 (12) (2005) 123516.
[49] X. Zhang, N. Li, O. Anderoglu, H. Wang, J.G. Swadener, T. Hochbauer, A. Misra, R.G. Hoagland, Nucl. Instrum. Methods Phys. Res. Sect. B – Beam Interact. Mater. Atoms 261 (1–2) (2007) 1129.
[50] M.J. Demkowicz, R.G. Hoagland, J.P. Hirth, Phys. Rev. Lett. 100 (13) (2008).
[51] 51 H.L. Heinisch, F. Gao, R.J. Kurtz, J. Nucl. Mater. 329–333 (2004) 924.
[52] E.G. Fu, J. Carter, G. Swadener, A. Misra, L. Shao, H. Wang, X. Zhang, J. Nucl. Mater. 385 (3) (2009) 629.
[53] M. Nastasi, J. Mayer, J.K. Hirvonen, Ion–Solid Interactions: Fundamentals and Applications, Cambridge, New York, 1996.
[54] J.F. Ziegler, U. Littmark, J.P. Biersack, Calculation using the Stopping and Range of Ions in Matter (SRIM) Code. <http://www.srim.org/>.
[55] E.A. Kenik, T.E. Mitchell, Philos. Mag. 32 (1975) 815.
[56] A.A. Lucas, Physica B&C 127 (1984) 225.
[57] H. Westendorp, Z.L. Wang, F.W. Saris, Nucl. Instrum. Methods Phys. Res. 194 (1–3) (1982) 453.
[58] M. van Rossum, U. Shreter, W.L. Johnson, M.-A. Nicolet, Mater. Res. Soc. Symp. Proc. 27 (1984) 127.
[59] N. Li, E.G. Fu, H. Wang, J.J. Carter, L. Shao, S.A. Maloy, A. Misra, X. Zhang, J. Nucl. Mater. 389 (2) (2009) 233.
[60] N. Li, M.S. Martin, O. Anderoglu, A. Misra, L. Shao, H. Wang, X. Zhang, J. Appl. Phys. 105 (12) (2009).
[61] B.M. Paine, R.S. Averback, Nucl. Instrum. Methods B 7–8 (1985) 666.
[62] F.R. de Boer, W.C.M. Mattens, A.R. Miedema, A.K. Niessen, Cohesion in Metal: Transition Metal Alloys, Amsterdam, North-Holland, 1989.
[63] T.B. Massalski, L.H. Bennett, H. Baker, Binary Alloy Phase Diagrams, American Society for Metals, Metals Park, 1986.
[64] E.G. Fu, N. Li, A. Misra, R.G. Hoagland, H. Wang, X. Zhang, Mater. Sci. Eng. A – Struct. Mater. Prop. Microstruct. Process. 493 (1–2) (2008) 283.
[65] S.J. Zinkle, Y. Matsukawa, J. Nucl. Mater. 329 (2004) 88.
[66] E. Alonso, M.J. Caturla, T.D. de la Rubia, J.M. Perlado, J. Nucl. Mater. 276 (2000) 221.
[67] R. Sizmann, J. Nucl. Mater. 69–70 (1968) 386.
[68] A. Misra, M.J. Demkowicz, X. Zhang, R.G. Hoagland, JOM 59 (9) (2007) 62.
[69] M.J. Caturla, N. Soneda, E. Alonso, B.D. Wirth, T.D. de la Rubia, J.M. Perlado, J. Nucl. Mater. 276 (2000) 13.
[70] J.P. Hirth, Theory of Dislocations, McGraw-Hill, New York, 1968.
[71] R.L. Mills, D.H. Liebenberg, J.C. Bronson, Phys. Rev. B 21 (11) (1980) 5137.
[72] A. Driessen, E. Vanderpoll, I.F. Silvera, Phys. Rev. B 33 (5) (1986) 3269.
[73] S.E. Donnelly, Radiat. Eff. Defects Solids 90 (1985) 1.
[74] T. Schober, R. Laser, J. Golczewdki, C. Dieker, H. Trinkaus, Phys. Rev. B 31 (1985) 7109.
[75] W.G. Wolfer, Philos. Mag. A 59 (1989) 87.
[76] G.E. Lucas, J. Nucl. Mater. 206 (2–3) (1993) 287.
[77] S.A.K., in: Second UN Conference on Peaceful Uses of Atomic Energy, vol. 6, 1958, New York, United Nations.
[78] J. Friedel, Dislocations, Pergamon, New York, 1964.
[79] F. Kroupa, P.B. Hirsch, Discuss. Faraday Soc. 38 (1964) 49.
[80] H. Ullmaier, E. Camus, J. Nucl. Mater. 251 (1997) 262.
[81] J.D. Hunn, E.H. Lee, T.S. Byun, L.K. Mansur, J. Nucl. Mater. 282 (2–3) (2000) 131.
[82] E.H. Lee, T.S. Byun, J.D. Hunn, K. Farrell, L.K. Mansur, J. Nucl. Mater. 296 (2001) 183.
[83] G.I. Taylor, J. Inst. Metals 62 (1938) 307.
[84] S. Timoshenko, 69th Anniversary Volume, MacMillan, New York, 1938.
[85] U.F. Kocks, J.C.M. Li, Can. J. Phys. 45 (1967) 1134.
[86] U.F. Kocks, Metall. Trans. 1 (1970) 1121.
[87] J.R. Cahoon, W.H. Broughton, A.R. Kutzak, Metall. Trans. 2 (1971) 1979.
[88] A. Misra, J.P. Hirth, R.G. Hoagland, Acta Mater. 53 (8) (2005) 4817.
[89] M.A. Krivoglaz, X-Ray and Neutron Diffraction in Non-ideal Crystals, Springer, Berlin, 1995.
[90] B.C. Larson, J. Appl. Phys. 45 (2) (1974) 514.